Controlling reaction-induced loss of active sites in ZnO_x/silicalite-1 for durable non-oxidative propane dehydrogenation

Dan Zhao[a, b†], Ke Guo[b†], Shanlei Han[a, b], Dmitry E. Doronkin[c], Henrik Lund[a], Jianshu Li[b], Jan-Dierk Grunwaldt[c], Zhen Zhao[b], Chunming Xu[b,d], Guiyuan Jiang[b], Evgenii V. Kondratenko[a*]*

[a]Leibniz-Institut für Katalyse e. V., Albert-Einstein-Strasse 29A, 18059 Rostock, Germany, *evgenii.kondratenko@catalysis.de (EVK)

[b]State Key Laboratory of Heavy Oil Processing, China University of Petroleum, Beijing, Beijing 102249, P. R. China, * jianggy@cup.edu.cn (GJ)

[c]Institute of Catalysis Research and Technology and Institute for Chemical Technology and Polymer Chemistry, Karlsruhe Institute of Technology (KIT), Engesserstr.20, 76131 Karlsruhe, Germany

[d]Haihe Laboratory of Sustainable Chemical Transformations, Tianjin 300192, P.R. China

†These authors contributed equally to this work.

KEYWORDS: ZnO_x/silicalite-1; Zn loss; MgO promoter; durability; non-oxidative propane dehydrogenation

ABSTRACT

ZnO-based catalysts are promising for the non-oxidative propane dehydrogenation (PDH) to propene owing to their low cost and environmental friendliness but experience serious loss of the active component because of the reduction of ZnO to metallic Zn that evaporates. Here, we demonstrate that MgO-modified ZnO_x/silicalte-1 materials prepared through one-pot hydrothermal method are active, selective, and durable in the PDH reaction. The undesired loss of Zn could also be successfully suppressed without negative effect on the PDH performance owing to a strong interaction between Mg^{2+} and ZnO_x as concluded from the results of X-ray photoelectron and Fourier-transform infrared spectroscopic measurements as well as temperature-programmed reduction with CO. X-ray absorption spectroscopy revealed that atomically dispersed Zn^{2+} sites are responsible for propane dehydrogenation. Using an industrially relevant feed with 40 vol% propane, propene selectivity between 88 and 95% at propane conversion between 15 and 32% was achieved over 6 PDH/oxidative regeneration cycles lasting for about 20 h on stream at 550 ˚C without loss in the initial activity, while some deactivation occurred after longer (up to about 60 h) time on stream. The deactivation (caused by Zn loss) constant of Mg-modified

ZnO_x/silicalite-1 considering the 2nd and 20th cycles is more than three times lower than that of its Mg-free counterpart.

INTRODUCTION

ZnO is a multipurpose material used for the production of batteries[1], pigments[2], foods[3] and even drugs[4]. It also can be used as a support or active component in heterogeneous catalysis[5-7], e.g. methanol synthesis[8-10] and steam-reforming of methanol[11-13] as well as in photocatalysis[14-16]. Owing to the great developments in synthesis and characterization techniques, varieties of ZnO nanostructures were synthesized, which are nanotubes[17-18], nanobars[19], nanosheets[20], nanoflowers[21-22] even quantum dots[23-24]. They are, however, widely employed in low-temperature (<300 ˚C) reactions since those nanostructures are prone to sintering at high temperatures. Moreover, ZnO can be reduced to metallic Zn at high temperatures in the presence of reducing agents. The metal melts at about 420 ˚C leading to sintering of small Zn aggregates or their evaporation. Thus, the application potential of ZnO-containing materials could be strengthened when methods for stabilizing certain Zn-containing structures or for hindering ZnO reducibility to metallic Zn are established.

Propene, an important building block in the chemical industry, can be produced through both oxidative and non-oxidative propane dehydrogenation[25-26]. The former one is usually carried out with an oxidizing agent that oxidizes not only propane to propene but also these hydrocarbons to

carbon oxides. Consequently, the selectivity to propene is low at industrially relevant degrees of propane conversion. Due to these reasons, the oxidative propane dehydrogenation is still not commercialized, while the non-oxidative propane dehydrogenation (PDH) to propene is the basis of several large-scale technologies[25-26]. The present commercially applied Pt-based or Cr-based catalysts have shortcomings related to the high-cost of platinum or toxicity of chromium(VI) compounds. To overcome these drawbacks, a multitude of alternative catalysts on the basis of oxides of Ga[27-28], V[29-31], Zr[32-36]or Sn[37-38] have been developed and tested in the PDH reaction.

ZnO-containing catalysts based on various supports such as Al_2O_3[39], SiO_2[40], HZSM-5[41], dealuminated Beta[42] and silicalite-1[43-45] were also widely studied. These catalysts show, however, industrially unattractive propene productivity due to either low propane conversion or low propene selectivity and have been tested using industrially irrelevant reaction feeds. Furthermore, reduction of ZnO to metallic Zn under reaction conditions lead to poor durability and irreversible deactivation of catalysts due to evaporation of the metal[41-42]. Very recently[46], we have introduced a simple method for preparation of highly active and selective Zn-containing catalysts under industrially relevant conditions. The most active developed catalyst shows about 3 times higher propene productivity in comparison with an analogue of commercial K-CrO_x/Al_2O_3. We merely

use a physical mixture of bulk ZnO and silicalite-1(S-1) as a catalyst. Catalytically active binuclear ZnO_x species are in situ formed through a reaction of metallic Zn atoms with OH nests upon reductive treatment or reaction conditions. Such species can, nevertheless, form metallic Zn that leaves the zeolite and reactor resulting in deactivation after about 250 h on propane stream. However, the active site and catalytic performance could be totally recovered by periodic adding of fresh ZnO on the top of catalyst bed. Depositing a nitrogen-doped carbon layer on S-1 support can help to stabilize ZnO_x species owing to the strong interaction between Zn and N species in the carbon layer[43]. Unfortunately, the developed catalysts are not compatible with oxidative regeneration required for removal of coke deposits formed in the PDH reaction since the protective layer is oxidized. Thus, new approaches for stabilizing ZnO_x species are highly needed.

Against the above background, the purpose of the present study was to provide a method for preparation of catalysts with improved thermal stability of ZnO_x under reducing conditions of the PDH reaction. The idea behind our approach is the easy formation of stable $ZnMgO_x$ solid solutions due to similarity of the ionic radii of Mg^{2+}(0.72 Å) and Zn^{2+}(0.74 Å)[47-48]. On this basis, we elucidated the potential of Mg-modification of ZnO_x/S-1. To verify this hypothesis, the designed catalysts were characterized by X-ray absorption spectroscopy (XAS), infrared

spectroscopy (IR), X-ray photoelectron spectroscopy (XPS), X-ray diffraction (XRD), and temperature-programmed reduction with carbon monoxide (CO-TPR). In contrast to major previous studies on the PDH reaction over Zn-containing catalysts, we determined catalyst activity, selectivity, and durability under industrially relevant conditions using a feed with 40 vol% propane as recommended in a recent review article[26].

EXPERIMENTAL

Chemicals and catalyst preparation

Ludox colloidal silica (40 wt%, Qingdao Haiyang Chemical Co., Ltd), tetrapropylammonium hydroxide (25 wt%, TPAOH, Shanghai Cairui Chemical Engineering Technology Co., Ltd), $Zn(NO_3)_2{\cdot}6H_2O$ (Sinopharm Chemical Reagent Co., Ltd), $Mg(NO_3)_2{\cdot}6H_2O$ (Guangfu Chemical Reagent Co.), $NH_3{\cdot}H_2O$ (25 wt%, ROTH) and ethylenediamine (Guangfu Chemical Reagent Co., Ltd) were used for catalyst preparation as received without any further purification.

ZnO/silicalite-1 samples were synthesized according to Ref. 49 but with some modifications. Briefly, the desired amounts of deionized water (40.56 g), $Zn(NO_3)_2{\cdot}6H_2O$ and ethylenediamine were mixed at 35 ˚C under continuous stirring. The molar ratio of ethylenediamine to Zn^{2+} was

fixed to 3. After 30 min stirring, 36 g of colloidal silica were added to the above solution and stirred for additional 30 min. Then, 40.99 g of TPAOH were added to the obtained suspension at 35 ˚C upon continuous stirring for aging for 6 h. Afterwards, the suspension was placed in a stainless-steel autoclave with a PTFE insert (200 ml) at 150 ˚C for 3 days. The formed solid product was collected by filtration, washed with deionized water, and then dried at 100 ˚C overnight and finally calcined at 550 ˚C for 6 h to remove the structure-directing agent. The samples are denoted as xZnO/S-1, where x stands for the theoretical loading of zinc in the weight percentage. The actual zinc loading was determined by ICP, which is 2.0, 3.9, 5.6 and 5.9 wt% in 2ZnO/S-1, 4ZnO/S-1, 6ZnO/S-1 and 8ZnO/S-1, respectively (Table 1). Bare slicalite-1 (named as S-1) was synthesized according to the same procedure but without addition of Zn source and ethylenediamine.

The same method was also used for preparation of a series of Mg-modified 6ZnO/S-1 samples. The required amounts of $Mg(NO_3)_2{\cdot}6H_2O$ and $Zn(NO_3)_2{\cdot}6H_2O$ were added into deionized water to achieve the molar ratio of Mg to Zn between 0.3 and 1.5. The amount of ethylenediamine was calculated according to the molar ratio of ethylenediamine to (Zn^{2+}+Mg^{2+}) of 3. The remaining steps were the same as described above for the preparation of the ZnO/S-1 materials. The Mg-containing samples are denoted as 6ZnO/S-1(yMg), where y stands for the molar ratio of Mg to

Zn in the initial gel. The actual molar ratio of Mg to Zn in the obtained samples is close to the nominal value (Table 1).

For comparative purposes, non-supported Mg-doped ZnO (Mg^{2+}:Zn^{2+}=1:1) was also synthesized according to Ref. 50 but with some modifications. $Zn(NO_3)_2 \cdot 6H_2O$ (5.00 g) and $Mg(NO_3)_2 \cdot 6H_2O$ (4.31 g) were dissolved in 50 ml H_2O. Oxalic acid (3.59 g) was dissolved in 50 ml H_2O at 60 ˚C. The pH value of Zn^{2+}- and Mg^{2+}-containing solutions was adjusted to the same pH value as that of the oxalic acid solution after adding of 2 M HNO_3. Both solutions were mixed under stirring and the pH value was adjusted to 9 by adding 25 wt% aqueous ammonia solution at 60 ˚C. The suspension was stirred at the same temperature for 1 h. The final catalyst was obtained after filtration, washing, drying and calcination at 550 ˚C for 4 h.

Catalyst characterization

Phase composition of as-prepared catalysts was determined by means of X-ray diffraction (XRD) measurements on an X'Pert Pro Theta/Theta diffractometer (Panalytical) with Cu Kα radiation (40 kV, 40 mA) in the 2θ range from 5 to 80 °. Peak positions and profile were fitted

with Pseudo-Voigt function using the HighScore Plus software package (Panalytical). Phase identification was done by using the PDF-2 database of the International Center of Diffraction Data (ICDD). Amorphous content was quantified according to the K-Factor approach implemented in the HighScore Plus software package using NIST 676 Al_2O_3 as external standard[51]. The crystallinity was calculated according to eq. 1.

$$\text{Crystallinity} = \frac{W_{crystalline}}{W_{crystalline} + W_{amorphous}} \times 100\% \quad \text{eq. 1}$$

, where $W_{crystalline}$ and $W_{amorphous}$ stand for the weight fractions of crystalline and amorphous phases in each sample, respectively.

The electronic state of Zn in the catalysts was analyzed by X-ray photoelectron spectroscopy (XPS) using a Thermo Fisher K-Alpha spectrometer. The electron binding energies were obtained after referencing the C1s core level of adventitious carbon at 284.6 eV.

Fourier transform infrared (FTIR) spectra of as-prepared samples were recorded on a Bruker VERTEX 70 equipped with DLaTGS detector in transmission mode. Each fresh sample was mixed with KBr with a weight ratio of 100(KBr):1(sample) and dried at 120 ˚C overnight followed by pressing into a self-supported wafer. The background spectrum was recorded using pure KBr and

automatically subtracted. All the FTIR spectra were recorded by accumulating 16 scans at a resolution of 4 cm^{-1}.

The reducibility of ZnO_x species was investigated by temperature-programmed reduction tests with carbon monoxide (CO-TPR) using an in-house developed setup containing 8 individually heated continuous-flow fixed-bed quartz reactors. Before reduction, each sample (50 mg) was heated in a flow of Ar to 550 ˚C followed by feeding air for 1 h and then cooling down to room temperature in air. The reduction was carried out in a flow of 1 vol% CO in Ar from room temperature to 900 ˚C with a heating rate of 10 ˚C/min. The CO (m/z=28), CO_2 (m/z=44) and H_2 (m/z=2) signals were detected by an on-line mass spectrometer.

The amount of coke over spent catalyst were determined by the temperature-programmed oxidation measurements with O_2 (O_2-TPO) using the same setup as applied for CO-TPR. Typically, 30 mg spent catalysts were loaded to reactors and flushed by Ar at room temperature for 30 min. The oxidation tests were carried out in a flow of 5 vol% O_2 in Ar with a heating rate of 10 ^oC/min from room temperature to 900 ^oC. The rate for coke formation was also determined based on the total amount of carbon deposition on the catalyst.

X-ray absorption near-edge spectra and extended X-ray absorption fine structure spectra (XANES and EXAFS) at the Zn K absorption edge were recorded at the P65 beamline of the PETRA III synchrotron (DESY, Hamburg) in transmission mode. The energy of the X-ray photons was selected by a Si (111) double-crystal monochromator and the beam size was set by means of slits to 0.2 (vertical) x 1.5 (horizontal) mm2. The spectra were normalized, and the extended X-ray absorption fine structure spectra (EXAFS) background was subtracted using the ATHENA program from the IFFEFIT software package[52]. The k^2-weighted EXAFS functions were Fourier transformed (FT) in the k range of 2.5-12.3 $Å^{-1}$. Then, the amplitude reduction factor S_0^2=1.05 was obtained by fitting the ZnO reference spectrum to a wurtzite structural model as reported in the Inorganic Crystal Structure Database (ICSD, collection code is 34477). The fits of the EXAFS data were performed using Artemis[52] by a least square method in R-space between 1.0 and 3.2 Å. The model with two shells from the wurtzite structure (Zn-O and Zn-Zn) was used for the fits. However, to fit the second shell with physically meaningful values, it was necessary to increase the starting interatomic distance for this shell by ca. 0.2 Å relative to the distance found in the original ZnO model. Thus, only first shell was considered here. Coordination numbers, interatomic

distances, energy shift (δE_0) and mean square deviation of interatomic distances (σ^2) were refined during fitting. The absolute misfit between theory and experiment was expressed by ρ.

Catalytic tests

Catalytic tests were performed using an in-house developed setup equipped with 15 fixed-bed quartz tubular reactors. Before testing, the as-synthesized catalysts were heated in N_2 flow of 10 ml·min^{-1} up to 550 ˚C, then they were treated in air followed by purging with N_2 for 15 min. Afterwards, N_2 was replaced by a feed consisting of 40 vol% C_3H_8 in N_2 with a total flow rate of 10 ml min^{-1}. To determine catalyst durability, i.e., the ability to restore initial activity after oxidative regeneration, PDH/regeneration tests were carried out as follows. The catalysts were tested in the PDH reaction at 550 ˚C for 2 h and then flushed with N_2 for 15 min. Then, air was fed to the reactors with a flow of 10 ml min^{-1} for 30 min at the same temperature. The oxidized catalysts were flushed with N_2 for 15 min and tested again in the PDH reaction for 2 h. In total, 20 PDH/regeneration cycles or 6 PDH/regeneration cycles were carried out over 6ZnO/S-1 and 6ZnO/S-1(1.0Mg) or 6ZnO/S-1(yMg) samples.

For determining the rate of propene formation, PDH tests with oxidatively or reductively treated catalysts were carried out at a degree of propane conversion below 10%. The catalysts (50 mg)

were initially treated in N_2 and air at 550 ˚C as described above. Hereafter, they were either directly used for PDH or reductively treated at 550 ˚C in a flow of 50 vol% H_2 in N_2 for 1 h and then applied for PDH. The rate was determined at the same temperature with a feed containing 40 vol% C_3H_8 in N_2 and a total flow rate of 40 ml min^{-1}. The rate of propene formation and turnover frequency (TOF) values of propene formation with respect to Zn were calculated according to eq. 2 and eq. 3, respectively.

$$r(C_3H_6) = \frac{\dot{n}_{C_3H_6}}{m_{cat}} \qquad \text{eq. 2}$$

$$TOF = \frac{r(C_3H_6)/60}{n_{Zn}} \qquad \text{eq. 3}$$

, where m_{cat} is the catalyst mass in gram and $\dot{n}_{C3H6}$ stands for the propene molar flow (mmol/min). n_{Zn} means the amount of Zn in m_{cat}.

The feed components and the reaction products were analyzed by an on-line gas chromatograph (Agilent 6890) equipped with flame ionization (FID) and thermal conductivity (TCD) detectors. The time for one analysis was 4 minutes. The gas chromatograph is equipped with PLOT/Q (for CO_2), AL/S (for hydrocarbons), and Molsieve 5 (for H_2, O_2, N_2, and CO) columns. Propane

conversion, propene selectivity, yield, and carbon balance were calculated according to eqs. 4-7, respectively.

$$X(C_3H_8) = \frac{\dot{n}^{in}_{C_3H_8} - \dot{n}^{out}_{C_3H_8}}{\dot{n}^{in}_{C_3H_8}} \quad \text{eq. 4}$$

$$S(C_3H_6) = \frac{\dot{n}^{out}_{C_3H_6}}{\dot{n}^{in}_{C_3H_8} - \dot{n}^{out}_{C_3H_8}} \quad \text{eq. 5}$$

$$Y(C_3H_6) = X(C_3H_8) \times S(C_3H_6) \quad \text{eq. 6}$$

$$B(C) = \frac{\dot{n}(CH_4)_{out} + 2\dot{n}(C_2H_6)_{out} + 2\dot{n}(C_2H_4)_{out} + 3\dot{n}(C_3H_8)_{out} + 3\dot{n}(C_3H_6)_{out}}{3\dot{n}(C_3H_8)_{in}} \times 100\% \quad \text{eq. 7}$$

where "$\dot{n}_{in}$" and "$\dot{n}_{out}$" stand for the molar flows of gas-phase components at the reaction inlet and outlet, respectively. N_2 was used as an inert standard to consider the reaction-induced changes in the number of molars. For all the tests, carbon balance values are above 97%.

The constant of catalyst deactivation due to Zn loss was calculated according to eq. 8. This equation was adapted from a previous study[53].

$$k_{deactivation} = \frac{\ln\left(\frac{1 - X(C_3H_8)_{20th}}{X(C_3H_8)_{20th}}\right) - \ln\left(\frac{1 - X(C_3H_8)_{1st\ or\ 2nd}}{X(C_3H_8)_{1st\ or\ 2nd}}\right)}{t} \quad \text{eq. 8}$$

To exclude the effect of coke deposition on Zn-loss related deactivation, we used the initial conversion of propane in the 1st cycle ($X(C_3H_8)_{1st}$) for 6ZnO/S-1, in the 2nd cycle ($X(C_3H_8)_{2nd}$) for 6ZnO/S-1(1.0Mg) and in the 20th cycle ($X(C_3H_8)_{20th}$) for both catalysts. The reason for choosing

the 2nd cycle for the MgO-containing sample is its activation behavior in the 1st cycle. t is the time on total propane stream, i.e., 40 and 38 hours for 6ZnO/S-1and 6ZnO/S-1(1.0Mg), respectively.

RESULTS AND DISCUSSION

General characterization of ZnO-based catalysts

To determine the crystalline phases in the developed catalysts with or without MgO, X-ray powder diffraction analysis was applied. In all samples, no crystalline ZnO could be identified. Neither crystalline MgO nor mixed MgO-ZnO phases could be detected in MgO-containing samples. Thus, ZnO and MgO should be highly dispersed.

The only identified crystalline phases are related to the zeolite support. Bare S-1 is present in the monoclinic structure (Figure 1a). This structure changes to the MFI polymorph with increasing amount of Zn-content in MgO-free samples as clearly indicated by the changes of diffraction data in the 2θ range between 23 and 25˚ (Figure 1a-c). Such changes could be caused by the presence of foreign cation or structure-directing agent, temperature, pressure and so on[54-55]. The Zn-related structural changes in our samples should not be caused by the incorporation of Zn into the framework of the zeolite due to the following reason. As reported in a previous study dealing with Mn-ZSM-5, the Bragg peaks in the 2θ range of 7-10 º shifts to lower values when manganese is

inside of the framework[56]. If zinc were present in the framework of our catalysts, a similar shift should be expected because the ionic radii of Mn^{2+} and Zn^{2+} are larger than the ionic radius of Si^{4+}. The Bragg peaks in the 2θ range of 7-10 ° in xZnO/S-1 samples remain at the same position as for S-1 (Figure 1b). Thus, ZnO_x species should be on the surface, i.e., in extra-framework positions.

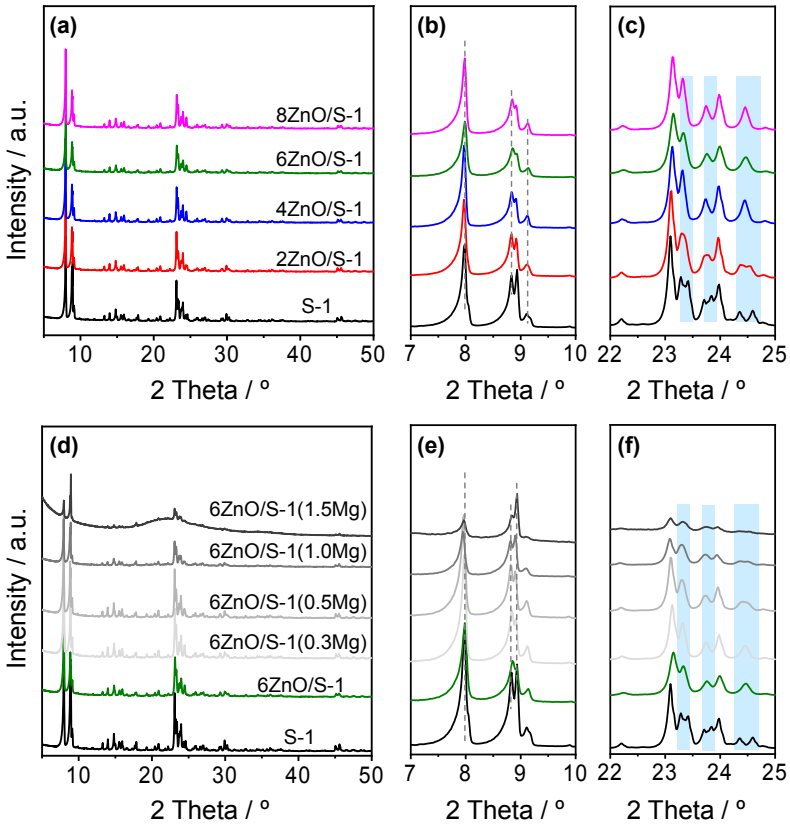

Figure 1 XRD patterns of as-prepared samples, (a) wide-angel XRD patters of S-1 and ZnO-containing samples; (b) magnified XRD patterns in the range of 2θ=7-10 °; (c) magnified XRD patterns in the range of 2θ=22-25 °; (d) wide-angel XRD patterns of S-1 and Mg-free and -

containing samples; (f) magnified XRD patterns in the range of 2θ=7-10 °; (e) magnified XRD patterns in the range of 2θ=22-25 °.

The orthorhombic MFI structure also maintains in the MgO-containing samples when the molar ratio of Mg/Zn is in the range of 0.3-1.0. When the ratio increases to 1.5, the structure collapses to a larger extent (Figure 1d). Regardless of the crystallinity of these samples, diffraction peaks indicate the presence of orthorhombic MFI structure (Figure 1e,f). The structural collapse in the 6ZnO/S-1(1.0Mg) sample can be explained as follows. Due to high amount of metal ions in the initial gel upon synthesis of S-1, the nucleation and crystalline processes were suppressed[57]. Hence, the crystallinity of the zeolites decreases with an increase in MgO loading (Figure 1d, Table 1).

The surface area of each sample was determined by means of N_2 adsorption-desorption measurements. Except for 6ZnO/S-1(1.0Mg) sample, the surface area of MgO-free and MgO-containing samples remains in the range of 340-381 m^2/g, where the area of the bare support is (Table 1). Thus, small amounts of metal ions in initial gel have no obvious effect on surface area. While when the ratio of Mg and Zn increases to 1.0, the surface area decreased significantly to 247 m^2/g. This should be due to the low crystallinity of this sample (Table 1). Too high Mg loading

is also detrimental for the surface area of micropores. It is 176 m^2 g^{-1} for the 6ZnO/S-1(1.0Mg) and in the range of 256-314 m^2 g^{-1} for all the other materials.

Table 1 The specific surface area (S(BET)), surface area of micropores (S(micropores)), relative crystallinity as well as Zn (w(Zn)) and Mg (w(Mg)) loading in as-synthesized samples. Zn loading in the spent materials was determined after 6 PDH/regeneration and 20 PDH/regeneration (in parentheses) cycles.

Samples	S(BET)/ $m^2 \cdot g^{-1}$	S(micropores)/ $m^2 \cdot g^{-1}$	Crystallinity (%)	Zn/wt% (fresh)[a]	Mg/wt% (fresh)[a]	Mg/Zn molar ratio	Zn/wt% (spent)[a]
S-1	363	314	90.3	0	0	-	-
2ZnO/S-1	381	308	83.7	2.0	0	-	-
4ZnO/S-1	376	284	80.0	3.9	0	-	-
6ZnO/S-1	350	264	71.3	5.6	0	-	4.9(4.0)
8ZnO/S-1	341	256	77.0	5.9	0	-	-
6ZnO/S-1(0.3Mg)	365	279	74.3	4.2	0.5	0.32	3.7
6ZnO/S-1(0.5Mg)	356	273	74.6	4.2	0.9	0.58	3.8
6ZnO/S-1(1.0Mg)	247	176	43.4	4.0	1.8	1.22	3.7(3.4)

a: Amounts of Zn and Mg were obtained by ICP

Catalytic performance

To check the effect of Zn loading in xZnO/S-1 on catalyst activity, the rate of propene formation was determined at 550 ˚C. Both bare S-1 and commercial ZnO were also tested for comparative purposes. The bare support is totally inactive, while commercial ZnO shows some activity (the rate is below 0.1 mmol·g^{-1}·min^{-1}, Figure S1 in the Supporting Information). The activity of ZnO_x/S-1 increases with Zn loading and reaches the highest value of 0.57 mmol·g^{-1}·min^{-1} over 6ZnO/S-1 and then decreases to 0.34 mmol·g^{-1}·min^{-1} over 8ZnO/S-1.

Based on the above screening test, a series of MgO-promoted 6ZnO/S-1 catalysts were prepared. The catalysts were tested for their activity in the PDH reaction after oxidative or reductive treatment. It is worth mentioning that in comparison with MgO-containing 6ZnO/S-1 catalysts, unsupported MgO-doped ZnO catalyst shows significantly lower activity (about 0.08 mmol·g^{-1}·min^{-1}). Thus, bulk Zn-O-Mg structure is inactive for propane dehydrogenation (Figure S2 in the Supporting Information). To fairly compare MgO-free and MgO-containing catalysts based on S-1, a TOF value of propene formation was calculated based on total amount of Zn in each sample according to eq. 3 and are shown in Figure 2. For the oxidized catalysts, this value for the MgO-free catalyst is 0.0116 s^{-1}, while the counterparts with the molar ratio of MgO/ZnO of 0.3 and 0.5 possess the values of 0.0137 and 0.0142 s^{-1}, respectively. The corresponding values for the reduced

catalysts are 0.011, 0.012 and 0.015 s^{-1}. The reduced 6ZnO/S-1(1.0Mg) catalyst has the TOF value of 0.0141 s^{-1}. Based on these results, no correlation between the activity and MgO content could be established. Thus, we put forward that all Mg-containing 6ZnO/S-1 catalysts have same ZnO_x active sites, and the presence of Mg does not affect their intrinsic activity. Additionally, no relationship could be determined between the TOF values and catalyst microporosity. Therefore, the micropores should not affect the catalytic performance.

The TOF value determined for the oxidatively treated 6ZnO/S-1(1.0Mg) is about 3 times lower than that over its reductively treated counterpart. We suppose that Zn species in 6ZnO/S-1(1.0Mg) need a reducing atmosphere to be activated. Such activation is common for catalysts based on metal oxides[41-42]. This assumption is supported by our results presented below.

The 6ZnO/S-1(yMg) catalysts were also tested in the PDH reaction for their durability at industrially relevant degrees of propane conversion. For their proper comparison, the contact time was selected to achieve about 30% initial propane conversion. The catalysts were oxidatively treated before the PDH reaction. Apart from 6ZnO/S-1(1.0Mg), which activates with rising time on propane stream in the first dehydrogenation cycle, all other catalysts deactivate (Figure 3). The deactivation should be due to coke formation[43]. Depending on MgO loading, the catalysts could

recover their initial activity to a different extent after oxidative removal of coke. The strongest loss in the initial conversion of propane from the 1st cycle to the 6th cycle was determined for the 6ZnO/S-1 sample, the corresponding conversion values are 29.6% and 22.2% (Figure 3a). According to our previous study[43], there are two mechanisms of deactivation of ZnO-based catalysts. Besides the reaction-induced formation of coke, which is responsible for the decrease in the activity with time on propane stream, Zn loss under PDH conditions is another reason for the deactivation with rising number of dehydrogenation/regeneration stages. The latter statement is supported by the present ICP results (Table 1). The loading of Zn in the 6ZnO/S-1 catalyst decreased from 5.6 to 4.9 wt% after 6 dehydrogenation/regeneration cycles. Importantly, the loss of Zn was suppressed when 6ZnO/S-1 was promoted by MgO. The higher the loading of MgO, the less pronounced Zn loss is (Table 1).

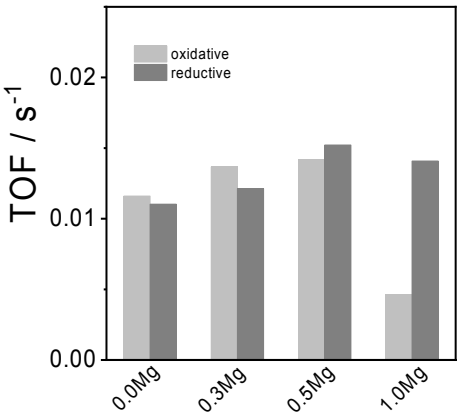

Figure 2 TOF values over 6ZnO/S-1(yMg) catalysts tested after oxidative (light grey bars) or reductive (dark grey bars) treatments. Reaction conditions: 550 ˚C, catalyst amount of 50 mg, C_3H_8:N_2=2:3, total flow rate of 40 ml·min^{-1}.

The positive effect of MgO on ZnO stabilization is also reflected in the higher catalyst durability. As seen in Figure 3b-d, the decrease in the initial propane conversion from cycle to cycle becomes less pronounced with an increase in MgO loading. The activity of 6ZnO/S-1(1.0Mg) in the last 5 cycles is fully recovered after removal of coke deposits in an air flow at 550 ^{o}C. Except for 6ZnO/S-1(1.0Mg) in the 1st PDH cycle, other catalysts showed similar selectivity to propene and coke, which are in the range of 88-95% and 3-10%, respectively (Figure S3 in the Supporting Information). Higher propene selectivity (about 92%) and lower coke selectivity (about 4%) were obtained over the 6ZnO/S-1(1.0Mg) sample in the 1st cycle in comparison with the other next cycles. This should be due to the lower conversion of propane. We also compared our catalysts with the state-of-the-art ZnO-based catalyst in terms of selectivity-conversion relationship for propene (Figure S4a in the Supporting Information). They show comparable propene selectivity at similar degree of propane conversion with however higher concentration of propane in feed.

It is also worth mentioning that many state-of-the-art ZnO-based catalysts were not evaluated for their durability[41-42, 44-45, 58-59]. There are only two reports, where such tests were carried out[42, 44]. Znβ-10 and Zn-4@S-1 catalysts were tested in 3 PDH/regeneration cycles at 550 °C or 600 °C using, however, diluted reaction feeds with 10 or 5 vol% propane. For example, propane conversion over Znβ-10 and Zn-4@S-1 significantly dropped after 2 PDH/regeneration cycles; from about 51% to 38%[42] and from about 30% to 23%, respectively.

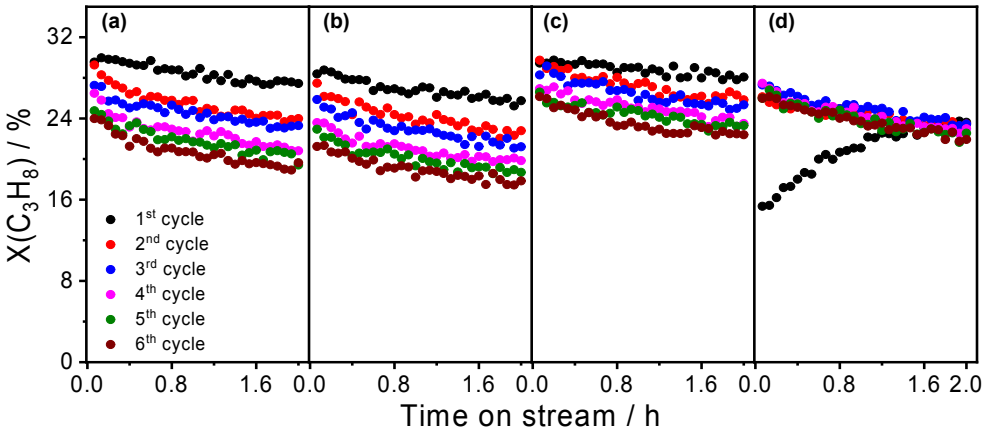

Figure 3 The PDH/regeneration behavior of MgO-free and MgO-promoted ZnO/S-1 catalysts. (a) 6ZnO/S-1; (b) 6ZnO/S-1(0.3Mg), (c) 6ZnO/S-1(0.5Mg), (d) 6ZnO/S-1(1.0Mg); reaction conditions: 200 mg catalyst, 550 °C, C_3H_8:N_2=2:3, total flow rate of 10 ml·min^{-1}, WHSV(propane)=2.1 h^{-1}. Regeneration conditions: 550 °C, 30 min, air flow (10 ml·min^{-1}).

For benchmarking purposes, our most promising 6ZnO/S-1(1.0Mg) catalyst was benchmarked against an analogue of commercial K-CrO_x/Al_2O_3 catalyst in terms of propene productivity. The highest space time yield of C_3H_6 formation in each PDH cycle are shown in Figure S4(b) in the Supporting Information. The activity of K-CrO_x/Al_2O_3 can be fully restored from cycle to cycle, while the 6ZnO/S-1(1.0Mg) deactivated to some extent. Nevertheless, 6ZnO/S-1(1.0Mg) shows higher STY(C_3H_6) than K-CrO_x/Al_2O_3.

To further demonstrate the effect of MgO on durability ZnO-based catalysts, the 6ZnO/S-1 and 6ZnO/S-1(1.0Mg) catalysts were also tested in 20 PDH/regeneration cycles. The obtained conversion and selectivity values are shown in Figure S5 in the Supporting Information. When comparing the 1st and the 20th cycle, the conversion of propane over 6ZnO/S-1 or 6ZnO/S-1(1.0Mg) decreases from 30.8% to 14.8% or from 26.1% (the initial conversion in 2nd cycle as it is the highest for this catalyst) to 20.9%. In addition, an apparent deactivation constant was calculated according to eq. 8 for 6ZnO/S-1(1.0Mg) and 6ZnO/S-1. The corresponding obtained values are 0.0076 h^{-1} and 0.0234 h^{-1}.

Temperature-programmed oxidation tests with O_2 (O_2-TPO) were carried out with spent catalysts (after 6 PDH/regeneration) to check if and how the presence of MgO effect coke

formation. The temperature of maximal rate of CO_2 formation over all catalysts is well below 550 °C and the combustion process is completed below 600 ˚C (Figure S6(a)). Taking these data into account and the fact that we used a feed with 20 vol% O_2 upon catalyst regeneration, we can safely conclude that coke formed in the PDH reaction is completely removed during the oxidative regeneration. An average rate of coke formation was calculated from the amount of CO_2 formed in the O_2-TPO tests (eq. 9). This rate decreases with an increase in MgO loading Figure S6(b) probably due to the basic properties of MgO. Thus, the role of MgO promoter for ZnO/S-1 is twofold: (i) thermal stability of ZnO_x species under reduction conditions is improved and (ii) coke formation is hindered.

$$\text{rate for coke formation} = \frac{\text{total amont of carbon deposition}}{m_{cat} \times t} \qquad \text{eq. 9}$$

where m_{cat} means the amount of catalyst used for PDH test, t is reaction time, i.e. 2 h on propane stream. The total amount of carbon deposition was determined from the amount of CO_2 formed upon O_2-TPO tests.

Nature of active ZnO_x sites

To derive an insight into the local structure of active ZnO_x species participating in propane dehydrogenation, X-ray absorption spectroscopy (XAS) was applied. The XANES spectra of the

as-synthesized catalysts, Zn foil and commercial ZnO are shown in Figure 4a. The latter two spectra are used as references for Zn oxidation states of 0 and +2, respectively. The position of the absorption edge in the XANES spectra of all catalysts is about 9662 eV, which is similar to that of commercial ZnO. Thus, the oxidation state of Zn in all as-synthesized catalysts should be +2. However, there is a shoulder at about 9673 eV in the spectrum of 6ZnO/S-1(1.0Mg), indicating that the electronic structure of Zn is different from that in the Mg-free sample. No Zn–Zn scattering on Zn neighbors as in metallic Zn (2.3 Å) is found in all the as-synthesized catalysts. Unlike commercial ZnO, the first-shell Zn–O scattering at about 1.5 Å (uncorrected distance) dominates in the spectra of 6ZnO/S-1 and 6ZnO/S-1(1.0Mg) samples, while the intensity of second shell of Zn–O is virtually non-visible suggesting the presence of atomically dispersed Zn^{2+} in both samples.

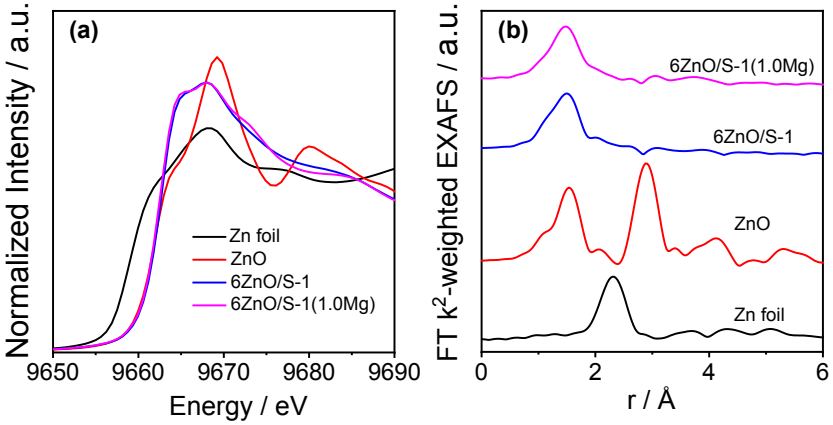

Figure 4 (a) XANES spectra and (b) FT EXAFS spectra (not corrected for the phase shift) of as-prepared samples and reference materials.

The Fourier transformed k^2-weighted extended X-ray adsorption fine structure (EXAFS) spectra are presented in Figure 4b (extracted EXAFS functions are given in Figure S7 in the Supporting Information). The EXAFS fitting parameters are summarized in Table 2, while the fits are reported in Figure S8 in the Supporting Information. The fitting data on binuclear Zn species in ZnO_x/S-1[46] identified in our previous work is provided for comparison in Table 2.

Since Zn-Zn distance and coordination number (CN) of Zn in 6ZnO/S-1 and 6ZnO/S-1(1.0Mg) could not be perfectly fitted, we put forward that Zn^{2+} species exists in the form of a single site. EXAFS is especially sensitive to interatomic distances and the significant difference here, as well as significantly higher disorder (Debye-Waller factor, σ^2) strongly suggest the absence of binuclear Zn species for 6ZnO/S-1 and 6ZnO/S-1(1.0Mg) samples. This difference between the EXAFS spectra of previously reported binuclear Zn sites and the 6ZnO/S-1 and 6ZnO/S-1(1.0Mg) is further illustrated in Figure S9 in the Supporting Information. In addition, the fitted CN of Zn-O is 3 instead of 4, with the latter being typical for Zn^{2+} inside the framework of the zeolite. Thus, isolated ZnO_x species should be located on the surface, in line with XRD results.

Table 2 EXAFS fitting parameters of as-synthesized catalysts and TOF values

Catalyst	Zn-O distance (Å)	CN (Zn-O)	σ^2 for O (10^{-3} Å^2)	Zn-Zn distance (Å)	CN (Zn-Zn)	δE_0 (eV)	ρ (%)	TOF value[b] / s^{-1}
6ZnO/S-1	1.967±0.008	3.4±0.2	8.3±1.2	n.f.[a]	n.f.[a]	2.3±0.7	0.3	0.011
6ZnO/S-1(1.0Mg)	1.976±0.009	3.3±0.3	9.2±1.5	n.f[a]	n.f.[a]	1.9±0.9	0.5	0.014
binuclear ZnO_x/S-1[c]	1.97±0.01	2.9±0.2	7.3±1.6	3.32±0.07	1.3±0.5	4.7±0.6	0.2	0.066

[a] n.f. means not fitting at these conditions.

[b] The TOF values were obtained over different samples after reductive treatment.

[c] The fitting data for binuclear ZnO_x/S-1 were took from Ref. 46.

Note: coordination numbers and distances in reference materials:

Zn metal: CN1(Zn-Zn)=6, r1(Zn-Zn)=2.665 Å; CN2(Zn-Zn)=6, r2(Zn-Zn)=2.913 Å..

Bulk ZnO: CN(Zn-O)=4, r(Zn-O)=1.970 Å, CN(Zn-Zn)=6, r(Zn-Zn)=3.213 Å, CN(Zn-Zn)=6, r(Zn-Zn)=3.250 Å

From a kinetic viewpoint, ZnO_x single sites in 6ZnO/S-1 and 6ZnO/S-1(1.0Mg) reveal about 5-6 times lower intrinsic activity expressed as Zn-related TOF in comparison with binuclear ZnO_x in S-1 reported in Ref.46; the TOF values are 0.011, 0.014 and 0.066 s^{-1}, respectively. This experimental result nicely supports our DFT calculations[46].

Origins of the MgO effect on thermal stability of ZnO

To explain why and how the presence of MgO affects the thermal stability of ZnO, we applied several techniques for characterizing selected catalysts. The FTIR spectra of the 6ZnO/S-1 and 6ZnO/S-1(1.0Mg) materials are shown in Figure 5a. The band located at about 450 cm^{-1} is attributed to the Zn-O stretching mode[50]. In comparison with the Mg-free sample, a blue-shift (from about 450 cm^{-1} to about 460 cm^{-1}) in the spectrum of 6ZnO/S-1(1.0Mg) should be especially noted. From a fundamental point of view, there are many factors that can affect the vibrational frequencies in IR spectroscopy, e. g. mass of the atoms, conjugate effect, or hydrogen bonding. For example, the vibrational frequencies are inversely proportional to the mass of the atoms according to Hooke's law, in other words, the bonds between lighter atoms have higher vibrational frequencies. In our case, such blue shift is mainly caused by the presence of Mg, which has lower relative atomic mass (24) than Zn (65). Thus, this result suggests that a Zn-O-Mg bond is formed in the 6ZnO/S-1(1.0Mg) sample[50, 60].

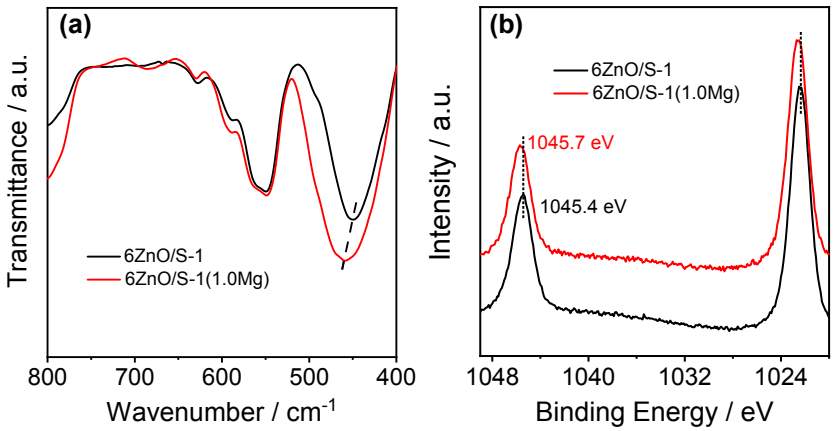

Figure 5 (a) FTIR spectra of 6ZnO/S-1 and 6ZnO/S-1(1.0Mg); (b) Zn 2p XP spectra of 6ZnO/S-1 and 6ZnO/S-1(1.0Mg).

Electronic properties of Zn in Mg-free and Mg-containing samples were also investigated by XPS. As seen in Figure 5b, there are two peaks at binding energy(BE) of about 1022 eV and 1045 eV, which are attributed to Zn $2p_{1/2}$ and Zn $2p_{3/2}$, respectively[61-62]. Compared to the 6ZnO/S-1 sample, the binding energy of Zn $2p_{1/2}$ and Zn $2p_{3/2}$ in 6ZnO/S-1(1.0Mg) is shifted to higher values from 1022.3 eV to 1022.6 eV and from 1045.4 eV to 1045.7 eV, respectively. The shift indicates that there should exist electronic interactions between Zn^{2+} and Mg^{2+}. Thus, combining the IR and XPS data, we can safely conclude that Mg^{2+} and Zn^{2+} are in proximity and strongly interacts with each other.

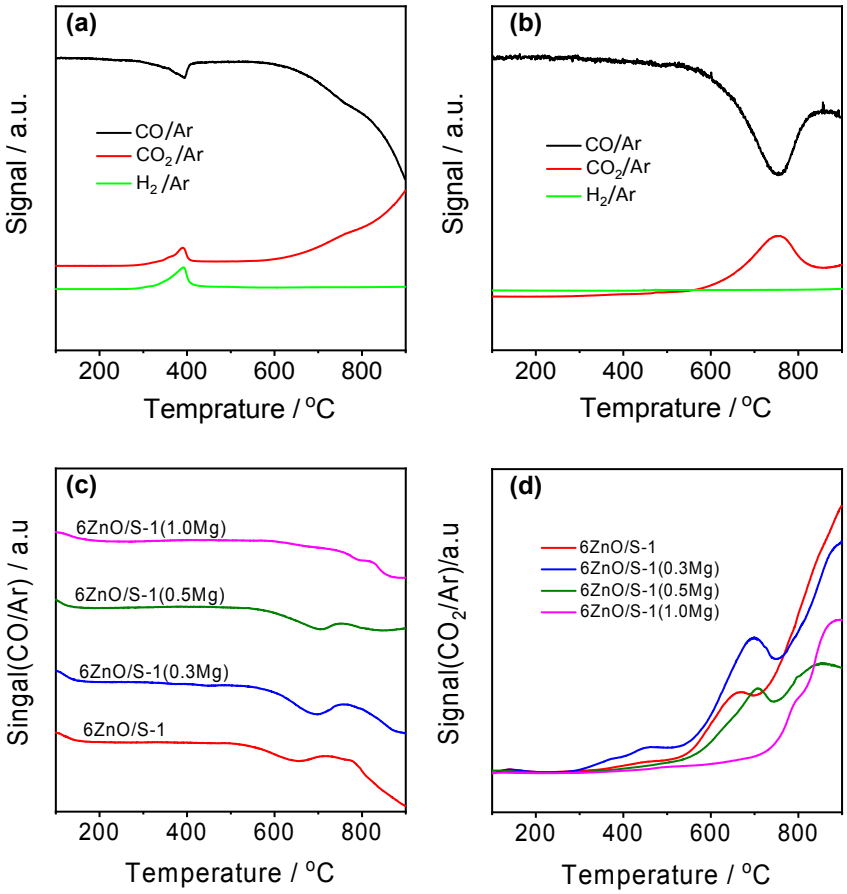

Figure 6 CO/Ar, CO_2/Ar and H_2/Ar profiles recorded upon CO-TPR measurements using (a) commercial ZnO oxidatively pre-treated at (a) 550 °C or (b) 800 °C. (c) CO/Ar signal, (d) CO_2/Ar signal of as-synthesized 6ZnO/S-1(yMg).

Further CO-TPR measurements were carried out to check the effect of MgO on reducibility of ZnO_x species. For comparative purposes, the reducibility of commercial ZnO was also studied. This metal oxide was oxidatively treated at either 550 or 800 °C before the CO-TPR tests (Figure 6a,b). The high-temperature treatment was necessary to remove surface OH groups. According to

Ref.[63], two different mechanisms are considered for CO reaction with metal oxides, i.e., removal of OH groups or lattice oxygen (eqs. 9 and 10). When ZnO was oxidatively treated at 550 °C and subsequently used for CO-TPR, CO consumption occurred in two temperature regions with the maximal rates at about 400 °C and above 600 °C. The low-temperature consumption of CO is accompanied by the formation of CO_2 and H_2 (Figure 6a). No H_2 is observed in the high-temperature region. This product is also not found in CO-TPR of ZnO treated oxidatively at 800 °C (Figure 6b). Based on these experimental observations and mechanistic concepts of CO reaction with metal oxides (eqs. 10 and 11), the low-temperature CO consumption in Figure 6a should be related to the removal of OH groups by CO, while lattice oxygen of ZnO reacts with CO above 600 °C.

$$2CO + 2OH - \rightarrow 2CO_2 + H_2 + 2O_{vacancy} \quad \text{eq. 10}$$

$$CO + Zn[O] \rightarrow CO_2 + O_{vacancy} \quad \text{eq. 11}$$

The CO, CO_2 and H_2 profiles recorded in CO-TPR tests with 6ZnO/S-1 and 6ZnO/S-1(yMg) are shown in Figure 6c,d and Figure S9 in the Supporting Information, respectively. MgO is not expected to be reduced under the conditions applied in our study. Thus, all CO consumption should be attributed to the reduction of ZnO_x species. It is obvious from Figure 6c that the temperature of

maximal CO consumption rate (T_{max}) is shifted to higher temperature with an increase in MgO loading. The corresponding value for 6ZnO/S-1, 6ZnO/S-1(0.3Mg), 6ZnO/S-1(0.5Mg) and 6ZnO/S-1(1.0Mg) is 655 °C, 698 °C, 709 °C and 792 °C, respectively. H_2 could be observed in CO-TPR measurements (Figure S10 in the Supporting Information). This indicates that OH groups probably connected to Zn^{2+} were removed by CO. Unlike the CO_2 signal (Figure 6d), the intensity of the H_2 signal decreases when the reduction temperature increases further. Therefore, we put forward that both reduction mechanisms are valid for 6ZnO/S-1 and Mg-promoted 6ZnO/S-1 samples and the continuous formation CO_2 should be attributed to the removal of oxygen coordinated with Zn atoms (Figure 6d). Based on these results, we can conclude that promoting of ZnO/S-1 with MgO inhibits reduction of ZnO_x during PDH reaction due to the strong interaction between ZnO and MgO.

CONCLUSION

The usage of magnesium as a promoter in one-pot synthesis of Mg-modified Zn^{2+}/silicalite-1 enables stabilization of Zn^{2+} against its reduction to metallic Zn^0 with the latter being responsible for the undesired loss of this metal under reducing conditions at high temperatures. The

stabilization effect relates to an increase in the strength of the Zn–O bond. Moreover, the method is also suitable for generation of atomically dispersed ZnO_x species even at a metal loading of about 6 wt%. Such species are responsible for the dehydrogenation of propane to propene. Owing to the structural stabilization of such species, catalyst durability in the PDH reaction is improved in comparison to Mg-free samples without changes in the activity and propene selectivity. The obtained results highlight the importance of controlling the structure and the local surrounding of highly dispersed ZnO_x species for designing active and stable ZnO-based catalysts for non-oxidative hydrocarbon conversion under industrially relevant conditions.

ASSOCIATED CONTENT

AUTHOR INFORMATION

Corresponding Author

Guiyuan Jiang- State Key Laboratory of Heavy Oil Processing, China University of Petroleum, Beijing, Beijing 102249, P. R. China; ORCID:0000-0003-1464-3368

E-Mail: jianggy@cup.edu.cn (GJ)

Evgenii V. Kontratenko- Leibniz-Institut für Katalyse e. V., Albert-Einstein-Strasse 29A, 18059 Rostock, Germany, ORCID: 0000-0003-0431-6937

E-Mail: evgenii.kondratenko@catalysis.de (EVK)

Author Contributions

E.V.K. initiated and led the whole project. E.V.K. and G.J. supervised and coordinated the project. D.Z. prepared all the catalysts, carried out catalytic tests, and some characterization measurements. K.G. performed IR and XPS measurements and analyzed the results. D.Z. and E.V.K. wrote the first draft. D.E.D. and J.D.G. performed XAS experiments and analyzed the results. H. L. carried out the XRD measurements and analyzed the results. All the authors discussed the results and improved the manuscript.

Notes

The authors declare no competing financial interest.

Supporting Information.

The supporting information, including catalytic performance, CO-TPR results, and EXAFS fitting results, is available free of charge.

Figure S1-9

ACKNOWLEDGEMENT

Financial support by Deutsche Forschungsgemeinschaft (KO 2261/8-1), the National Natural Science Foundation of China (Grant Nos 21961132026, 21878331 and 91645108), the National Key Research and Development Program (Nos. 2020YFA0210903, 2021YFA1501304) and the Haihe Laboratory of Sustainable Chemical Transformations, and Science Foundation of China University of Petroleum, Beijing (C201604) and the State of Mecklenburg-Vorpommern are gratefully acknowledged. The authors also thank Anja Simmula for ICP measurements. Dr. D. Zhao. acknowledges support from the China Scholarship Council. We acknowledge DESY (Hamburg, Germany), a member of the Helmholtz Association HGF, for the prevision of experimental facilities. Parts of this research were carried out at PETER III and we would like to thank Dr. Edmund Welter for assistance in using beamline P65.

REFERENCES

1. Hou, L.; Lian, L.; Zhang, L.; Pang, G.; Yuan, C.; Zhang, X., Self-Sacrifice Template Fabrication of Hierarchical Mesoporous Bi-Component-Active ZnO/$ZnFe_2O_4$ Sub-Microcubes as Superior Anode Towards High-Performance Lithium-Ion Battery. *Appl. Catal. B.* **2015**, 25 (2), 238-246.

2. Kiomarsipour, N.; Shoja Razavi, R.; Ghani, K.; Kioumarsipour, M., Evaluation of shape and size effects on optical properties of ZnO pigment. *Appl. Surf. Sci.* **2013**, 270, 33-38.

3. Shi, L. E.; Li, Z. H.; Zheng, W.; Zhao, Y. F.; Jin, Y. F.; Tang, Z. X., Synthesis, antibacterial activity, antibacterial mechanism and food applications of ZnO nanoparticles: a review. *Food Addit. Contam. Part A Chem. Anal. Control Expo. Risk Assess* **2014**, 31 (2), 173-86.

4. Muhammad, F.; Guo, M.; Qi, W.; Sun, F.; Wang, A.; Guo, Y.; Zhu, G., pH-Triggered controlled drug release from mesoporous silica nanoparticles via intracelluar dissolution of ZnO nanolids. *J. Am. Chem. Soc.* **2011**, 133 (23), 8778-81.

5. M. L. Cubeiro; Fierro, J. L. G., Selective production of hydrogen by partial oxidation of methanol over ZnO-supported palldium catalysts. *J. Catal.* **1998**, 179, 150–162.

6. Liu, X.; Liu, M. H.; Luo, Y. C.; Mou, C. Y.; Lin, S. D.; Cheng, H.; Chen, J. M.; Lee, J. F.; Lin, T. S., Strong metal-support interactions between gold nanoparticles and ZnO nanorods in CO oxidation. *J. Am. Chem. Soc.* **2012**, 134 (24), 10251-8.

7. Yang, Y.; Ma, J.; Wu, F., Production of hydrogen by steam reforming of ethanol over a Ni/ZnO catalyst. *Int. J. Hydrog.* **2006**, 31 (7), 877-882.

8. Kurtz, M.; Strunk, J.; Hinrichsen, O.; Muhler, M.; Fink, K.; Meyer, B.; Woll, C., Active sites on oxide surfaces: ZnO-catalyzed synthesis of methanol from CO and H_2. *Angew. Chem., Int. Ed.* **2005**, 44 (18), 2790-2794.

9. Schur, M.; Bems, B.; Dassenoy, A.; Kassatkine, I.; Urban, J.; Wilmes, H.; Hinrichsen, O.; Muhler, M.; Schlogl, R., Continuous coprecipitation of catalysts in a micromixer: nanostructured Cu/ZnO composite for the synthesis of methanol. *Angew. Chem., Int. Ed.* **2003**, 42 (32), 3815-7.

10. Malte Behrens, F. S., Igor Kasatkin; Stefanie Kühl, M. H., Frank Abild-Pedersen, Stefan Zander, Frank Girgsdies, Patrick Kurr, Benjamin-Louis Kniep, Michael Tovar Richard W. Fischer Jens K. Nørskov, Robert Schlögl, The active site of methanol synthesis over Cu/ZnO/Al_2O_3 inductrial catalysts. *Science* **2012**, 336, 893-897.

11. Chang, C.-C.; Hsu, C.-C.; Chang, C.-T.; Chen, Y.-P.; Liaw, B.-J.; Chen, Y.-Z., Effect of noble metal on oxidative steam reforming of methanol over CuO/ZnO/Al_2O_3 catalysts. *Int. J. Hydrog.* **2012**, 37 (15), 11176-11184.

12. Llorca, J.; de la Piscina, P. R. r.; Dalmon, J.-A.; Sales, J.; Homs, N. s., CO-free hydrogen from steam-reforming of bioethanol over ZnO-supported cobalt catalysts. *Appl. Catal. B.* **2003**, 43 (4), 355-369.

13. Günter, M. M.; Ressler, T.; Jentoft, R. E.; Bems, B., Redox Behavior of Copper Oxide/Zinc Oxide Catalysts in the Steam Reforming of Methanol Studied by in Situ X-Ray Diffraction and Absorption Spectroscopy. *J. Catal.* **2001**, 203 (1), 133-149.

14. Lu, F.; Cai, W.; Zhang, Y., ZnO Hierarchical Micro/Nanoarchitectures: Solvothermal Synthesis and Structurally Enhanced Photocatalytic Performance. *Appl. Catal. B.* **2008**, 18 (7), 1047-1056.

15. Lv, Y.; Pan, C.; Ma, X.; Zong, R.; Bai, X.; Zhu, Y., Production of visible activity and UV performance enhancement of ZnO photocatalyst via vacuum deoxidation. *Appl. Catal. B.* **2013**, 138-139, 26-32.

16. Sirelkhatim, A.; Mahmud, S.; Seeni, A.; Kaus, N. H. M.; Ann, L. C.; Bakhori, S. K. M.; Hasan, H.; Mohamad, D., Review on Zinc Oxide Nanoparticles: Antibacterial Activity and Toxicity Mechanism. *Nanomicro Lett* **2015**, 7 (3), 219-242.

17. Alex B. F. Martinson; Jeffrey W. Elam, J. T. H., Michael J. Pellin, ZnO nanotube based dye-sensitized solar cells. *Nanoletter* **2007**, 7, 2183-2187.

18. Sun, Y.; Fuge, G. M.; Fox, N. A.; Riley, D. J.; Ashfold, M. N. R., Synthesis of Aligned Arrays of Ultrathin ZnO Nanotubes on a Si Wafer Coated with a Thin ZnO Film. *Adv. Mater.* **2005**, 17 (20), 2477-2481.

19. Portillo-Vélez, N. S.; Hernández-Gordillo, A.; Bizarro, M., Morphological effect of ZnO nanoflakes and nanobars on the photocatalytic dye degradation. *Catal. Today* **2017**, 287, 106-112.

20. Chen, S. J.; Liu, Y. C.; Shao, C. L.; Mu, R.; Lu, Y. M.; Zhang, J. Y.; Shen, D. Z.; Fan, X. W., Structural and Optical Properties of Uniform ZnO Nanosheets. *Adv. Mater.* **2005**, 17 (5), 586-590.

21. Kim, Y. J.; Yoo, J.; Kwon, B. H.; Hong, Y. J.; Lee, C. H.; Yi, G. C., Position-controlled ZnO nanoflower arrays grown on glass substrates for electron emitter application. *Nanotechnology* **2008**, 19 (31), 315202.

22. Park, J. K.; Kim, Y. J.; Yeom, J.; Jeon, J. H.; Yi, G. C.; Je, J. H.; Hahn, S. K., The topographic effect of zinc oxide nanoflowers on osteoblast growth and osseointegration. *Adv. Mater.* **2010**, 22 (43), 4857-61.

23. Nick S. Norberg, K. R. K., James E. Amonette, Ravi K. Kukkadapu, Dana A. Schwartz, Daniel R. Gamelin, Synthesis of colloidal Mn^{2+}-ZnO quantum dots and high-Tc derromagnetic nanocrystalline thin films. *J. Am. Chem. Soc.* **2004**, 126, 9387-9398.

24. Pavle V. Radovanovic; Nick S. Norberg, K. E. M., Daniel R. Gamelin, Colloidal transition-metal-doped ZnO quantum dots. *J. Am. Chem. Soc.* **2002**, 124, 15192-15193.

25. Sattler, J. J.; Ruiz-Martinez, J.; Santillan-Jimenez, E.; Weckhuysen, B. M., Catalytic dehydrogenation of light alkanes on metals and metal oxides. *Chem. Rev.* **2014**, 114 (20), 10613-53.

26. Otroshchenko, T.; Jiang, G.; Kondratenko, V. A.; Rodemerck, U.; Kondratenko, E. V., Current status and perspectives in oxidative, non-oxidative and CO_2-mediated dehydrogenation of propane and isobutane over metal oxide catalysts. *Chem Soc Rev* **2021**, 50 (1), 473-527.

27. Choi, S.-W.; Kim, W.-G.; So, J.-S.; Moore, J. S.; Liu, Y.; Dixit, R. S.; Pendergast, J. G.; Sievers, C.; Sholl, D. S.; Nair, S.; Jones, C. W., Propane dehydrogenation catalyzed by gallosilicate MFI zeolites with perturbed acidity. *J. Catal.* **2017**, 345, 113-123.

28. Sattler, J. J.; Gonzalez-Jimenez, I. D.; Luo, L.; Stears, B. A.; Malek, A.; Barton, D. G.; Kilos, B. A.; Kaminsky, M. P.; Verhoeven, T. W.; Koers, E. J.; Baldus, M.; Weckhuysen, B. M., Platinum-promoted Ga/Al_2O_3 as highly active, selective, and stable catalyst for the dehydrogenation of propane. *Angew. Chem., Int. Ed.* **2014**, 53 (35), 9251-6.

29. Liu, G.; Zhao, Z.-J.; Wu, T.; Zeng, L.; Gong, J., Nature of the Active Sites of VO_x/Al_2O_3 Catalysts for Propane Dehydrogenation. *ACS Catal.* **2016**, 6 (8), 5207-5214.

30. Zhao, Z. J.; Wu, T.; Xiong, C.; Sun, G.; Mu, R.; Zeng, L.; Gong, J., Hydroxyl-Mediated Non-oxidative Propane Dehydrogenation over VO_x/gamma-Al_2O_3 Catalysts with Improved Stability. *Angew. Chem., Int. Ed.* **2018**, 57 (23), 6791-6795.

31. Wu, T.; Liu, G.; Zeng, L.; Sun, G.; Chen, S.; Mu, R.; Agbotse Gbonfoun, S.; Zhao, Z.-J.; Gong, J., Structure and catalytic consequence of Mg-modified VO_x/Al_2O_3 catalysts for propane dehydrogenation. *AIChE Journal* **2017**, 63 (11), 4911-4919.

32. Otroshchenko, T.; Kondratenko, V. A.; Rodemerck, U.; Linke, D.; Kondratenko, E. V., ZrO_2-based unconventional catalysts for non-oxidative propane dehydrogenation: Factors determining catalytic activity. *J. Catal.* **2017**, 348, 282-290.

33. Otroshchenko, T.; Sokolov, S.; Stoyanova, M.; Kondratenko, V. A.; Rodemerck, U.; Linke, D.; Kondratenko, E. V., ZrO_2-Based Alternatives to Conventional Propane Dehydrogenation Catalysts: Active Sites, Design, and Performance. *Angew. Chem., Int. Ed.* **2015**, 54 (52), 15880-3.

34. Otroshchenko, T. P.; Kondratenko, V. A.; Rodemerck, U.; Linke, D.; Kondratenko, E. V., Non-oxidative dehydrogenation of propane, n-butane, and isobutane over bulk ZrO_2-based catalysts: effect of dopant on the active site and pathways of product formation. *Catal. Sci. Tech.* **2017**, 7 (19), 4499-4510.

35. Zhang, Y.; Zhao, Y.; Otroshchenko, T.; Lund, H.; Pohl, M. M.; Rodemerck, U.; Linke, D.; Jiao, H.; Jiang, G.; Kondratenko, E. V., Control of coordinatively unsaturated Zr sites in ZrO_2 for efficient C-H bond activation. *Nat Commun* **2018**, 9 (1), 3794.

36. Zhang, Y.; Zhao, Y.; Otroshchenko, T.; Han, S.; Lund, H.; Rodemerck, U.; Linke, D.; Jiao, H.; Jiang, G.; Kondratenko, E. V., The effect of phase composition and crystallite size on activity and selectivity of ZrO_2 in non-oxidative propane dehydrogenation. *J. Catal.* **2019**, 371, 313-324.

37. Wang, G.; Zhang, H.; Wang, H.; Zhu, Q.; Li, C.; Shan, H., The role of metallic Sn species in catalytic dehydrogenation of propane: Active component rather than only promoter. *J. Catal.* **2016**, 344, 606-608.

38. Wang, G.; Zhang, H.; Zhu, Q.; Zhu, X.; Li, X.; Wang, H.; Li, C.; Shan, H., Sn-containing hexagonal mesoporous silica (HMS) for catalytic dehydrogenation of propane: An efficient strategy to enhance stability. *J. Catal.* **2017**, 351, 90-94.

39. Liu, G.; Zeng, L.; Zhao, Z.-J.; Tian, H.; Wu, T.; Gong, J., Platinum-Modified ZnO/Al_2O_3 for Propane Dehydrogenation: Minimized Platinum Usage and Improved Catalytic Stability. *ACS Catal.* **2016**, 6 (4), 2158-2162.

40. Schweitzer, N. M.; Hu, B.; Das, U.; Kim, H.; Greeley, J.; Curtiss, L. A.; Stair, P. C.; Miller, J. T.; Hock, A. S., Propylene Hydrogenation and Propane Dehydrogenation by a Single-Site Zn^{2+} on Silica Catalyst. *ACS Catal.* **2014**, 4 (4), 1091-1098.

41. Chen, C.; Sun, M.; Hu, Z.; Ren, J.; Zhang, S.; Yuan, Z.-Y., New insight into the enhanced catalytic performance of ZnPt/HZSM-5 catalysts for direct dehydrogenation of propane to propylene. *Catal. Sci. Tech.* **2019**, 9 (8), 1979-1988.

42. Chen, C.; Hu, Z.; Ren, J.; Zhang, S.; Wang, Z.; Yuan, Z.-Y., ZnO Nanoclusters Supported on Dealuminated Zeolite β as a Novel Catalyst for Direct Dehydrogenation of Propane to Propylene. *ChemCatChem* **2019**, 11 (2), 868-877.

43. Zhao, D.; Li, Y.; Han, S.; Zhang, Y.; Jiang, G.; Wang, Y.; Guo, K.; Zhao, Z.; Xu, C.; Li, R.; Yu, C.; Zhang, J.; Ge, B.; Kondratenko, E. V., ZnO Nanoparticles Encapsulated in Nitrogen-Doped Carbon Material and Silicalite-1 Composites for Efficient Propane Dehydrogenation. *iScience* **2019**, 13, 269-276.

44. Xie, L.; Wang, R.; Chai, Y.; Weng, X.; Guan, N.; Li, L., Propane dehydrogenation catalyzed by in-situ partially reduced zinc cations confined in zeolites. *J. Energy Chem.* **2021**, 63, 262-269.

45. Liu, J.; Liu, Y.; Liu, H.; Fu, Y.; Chen, Z.; Zhu, W., Silicalite-1 Supported ZnO as an Efficient Catalyst for Direct Propane Dehydrogenation. *ChemCatChem* **2021**, 13 (22), 4780-4786.

46. Zhao, D.; Tian, X.; Doronkin, D. E.; Han, S.; Kondratenko, V. A.; Grunwaldt, J. D.; Perechodjuk, A.; Vuong, T. H.; Rabeah, J.; Eckelt, R.; Rodemerck, U.; Linke, D.; Jiang, G.; Jiao, H.; Kondratenko, E. V., In situ formation of ZnO_x species for efficient propane dehydrogenation. *Nature* **2021**, 599 (7884), 234-238.

47. Schumann, J.; Eichelbaum, M.; Lunkenbein, T.; Thomas, N.; Álvarez Galván, M. C.; Schlögl, R.; Behrens, M., Promoting Strong Metal Support Interaction: Doping ZnO for Enhanced Activity of Cu/ZnO:M (M = Al, Ga, Mg) Catalysts. *ACS Catal.* **2015**, 5 (6), 3260-3270.

48. Heiba, Z. K.; Arda, L., Structural properties of $Zn_{1-x}Mg_xO$ nanomaterials prepared by sol-gel method. *Cryst. Res. Technol.* **2009**, 44 (8), 845-850.

49. Otto, T.; Zones, S. I.; Hong, Y.; Iglesia, E., Synthesis of highly dispersed cobalt oxide clusters encapsulated within LTA zeolites. *J. Catal.* **2017**, 356, 173-185.

50. Etacheri, V.; Roshan, R.; Kumar, V., Mg-doped ZnO nanoparticles for efficient sunlight-driven photocatalysis. *ACS Appl. Mater. Interfaces* **2012**, 4 (5), 2717-25.

51. Brian H. O'Connor; Raven, M. D., Application of the Rietveld Refinement Procedure in Assaying Powdered Mixtures. *Powder Diffr.* **1988** 3,2-6.

52. Ravel, B.; Newville, M., ATHENA, ARTEMIS, HEPHAESTUS: data analysis for X-ray absorption spectroscopy using IFEFFIT. *J. Synchrotron Radiat.* **2005**, 12, 537-541.

53. Qi, L.; Babucci, M.; Zhang, Y.; Lund, A.; Liu, L.; Li, J.; Chen, Y.; Hoffman, A. S.; Bare, S. R.; Han, Y.; Gates, B. C.; Bell, A. T., Propane Dehydrogenation Catalyzed by Isolated Pt Atoms in identical withSiOZn-OH Nests in Dealuminated Zeolite Beta. *J Am Chem Soc* **2021**, 143 (50), 21364-21378.

54. Wu, E. L.; Lawton, S. L.; Olson, D. H.; Jr, A. C. R.; Kokotallo, G. T., ZSM-5 Type metarials: Factors affecting crystal symmetry. *J. Phys. Chem.* **1997**, 83, 2777-2781.

55. Lempesis, N.; Smatsi, N.; Mavrantzas, V. G.; Pratsinis, S. E., Pressure- and Temperature-Induced Monoclinic-to-Orthorhombic Phase Transition in Silicalite-1. *J. Phys. Chem. C .* **2018**, 122 (11), 6217-6229.

56. Meng, Y.; Genuino, H. C.; Kuo, C. H.; Huang, H.; Chen, S. Y.; Zhang, L.; Rossi, A.; Suib, S. L., One-step hydrothermal synthesis of manganese-containing MFI-type zeolite, Mn-ZSM-5,

characterization, and catalytic oxidation of hydrocarbons. *J. Am. Chem. Soc.* **2013**, 135 (23), 8594-605.

57. Lai, Y.; Rutigliano, M. N.; Veser, G., Controlled Embedding of Metal Oxide Nanoparticles in ZSM-5 Zeolites through Preencapsulation and Timed Release. *Langmuir* **2015**, 31 (38), 10562-72.

58. Han, S.; Zhao, D.; Lund, H.; Rockstroh, N.; Bartling, S.; Doronkin, D. E.; Grunwaldt, J.-D.; Gao, M.; Jiang, G.; Kondratenko, E. V., TiO_2-Supported catalysts with ZnO and ZrO_2 for non-oxidative dehydrogenation of propane: mechanistic analysis and application potential. *Catal. Sci. Tech.* **2020**, 10 (20), 7046-7055.

59. Sun, Y.; Gao, C.; Tao, L.; Wang, G.; Han, D.; Li, C.; Shan, H., Zn-Nb-O catalysts for propylene production via catalytic dehydrogenation of propane. *Catal. Commun.* **2014**, 50, 73-77.

60. Singh, J.; Kumar, P.; Hui, K. S.; Hui, K. N.; Ramam, K.; Tiwari, R. S.; Srivastava, O. N., Synthesis, band-gap tuning, structural and optical investigations of Mg doped ZnO nanowires. *CrystEngComm* **2012**, 14 (18).

61. Ma, H.; Han, J.; Fu, Y.; Song, Y.; Yu, C.; Dong, X., Synthesis of visible light responsive ZnO–ZnS/C photocatalyst by simple carbothermal reduction. *Appl. Catal. B.* **2011**, 102 (3-4), 417-423.

62. Aksoy, S.; Caglar, Y.; Ilican, S.; Caglar, M., Sol–gel derived Li–Mg co-doped ZnO films: Preparation and characterization via XRD, XPS, FESEM. *J. Alloys Compd.* **2012**, 512 (1), 171-178.

63. Kouva, S.; Honkala, K.; Lefferts, L.; Kanervo, J., Review: monoclinic zirconia, its surface sites and their interaction with carbon monoxide. *Catal. Sci. Tech.* **2015**, 5 (7), 3473-3490.

TOC

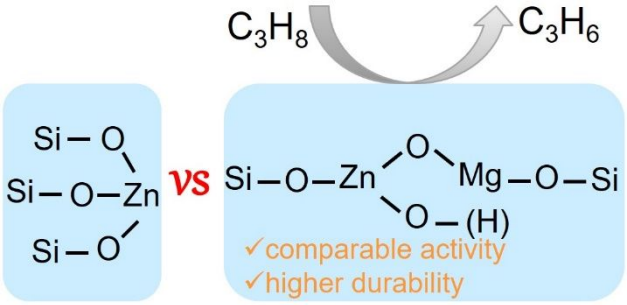
C3H8
C3H6
Si – O
Si – O – Zn
Si – O
vs
Si – O – Zn
O
Mg – O – Si
O – (H)
✓comparable activity
✓higher durability